# Journal of Materials Chemistry A

Accepted Manuscript






ROYAL SOCIETY OF CHEMISTRY

www.rsc.org/materialsA

Journal Name

ARTICLE

# A POM-Organic Framework Anode for Li-Ion Battery

Yanfeng Yue,[*,a,b] Yunchao Li,[a,c] Zhonghe Bi,[a] Gabriel M. Veith,[d] Craig A. Bridges,[a] Bingkun Guo,[a] Jihua Chen,[e] David R. Mullins,[a] Sumedh P. Surwade,[a] Shannon M. Mahurin,[a] Hongjun Liu,[a] M. Parans Paranthaman,[a,c] and Sheng Dai[*,a,f]

Received 00th January 20xx,
Accepted 00th January 20xx

DOI: 10.1039/x0xx00000x

www.rsc.org/

Rechargeable Li-ion batteries (LIBs) are currently the dominant power source for portable electronic devices and electric vehicles, and for small-scale stationary energy storage. However, one bottleneck of the anode materials for LIBs is the poor cycling performance caused by the fact that the anodes cannot maintain their integrity over several charge-discharge cycles. In this work, we demonstrate an approach to improving the cycling performance of lithium-ion battery anodes by constructing an extended 3D network of flexible redox active polyoxometalate (POM) clusters with redox active organic linkers, herein described as POMOF. This architecture enables the accommodation of large volume changes during cycling at relatively high current rates. For example, the POMOF anode exhibits a high reversible capacity of 540 mAh $g^{-1}$ after 360 cycles at a current rate of 0.25 C and a long cycle life at a current rate of 1.25C (> 500 cycles).

## 1. Introduction

A major impendent to the incorporation of new high-capacity anode materials for Li-ion batteries (LIBs) is their structural integrity over extended discharge–charge cycles. This problem has been attributed to the large volume changes during repeated lithium insertion and extraction reactions, which cause crumbling and cracking of the electrode, that leads to electrical disconnection from the current collectors.[1–5] Therefore, tremendous efforts have been devoted to solving the stability problems such as decreasing the dimensions of electrode materials to the nanoscale to mitigate the physical strains and minimize losses.[6–11] Another effective way of improving the cycling performance is making composites that use carbon and/or other inactive components as buffers [12–14], or organic ionic plastic crystals,[15,16] a new type of electrolytes, which have been proved as effective methods of strengthening the cycling stability. This improvement comes at the cost of a lower overall energy. In addition, the preparation of composite anodes usually involves multi-step synthesis, adding to preparation costs and time. In this work, we propose a new electrode architecture built from redox active linkers and polyoxometalate (POM) cluster species. This architecture has an intrinsic pore structure enabling diffusion as well as accommodating volume changes. Furthermore, the organic ligands function as buffers like the carbon and/or other inactive components in composite electrode materials.

This chemistry should not be confused with the typical metal-organic framework (MOF) materials[17–35] which are composed of molecular-type redox sites and multidentate organic ligands. MOF's such as lithium terephthalate have been used as anode materials for LIBs with an initial capacity of 300 mAh $g^{-1}$ and a capacity retention of 78% after 50 cycles.[36] More recently, MOF electrodes based on 1,4,5,8-naphthalenetetracarboxylate (NTC) ligand, namely, Li-NTC and Ni-NTC, were reported, with discharge and charge capacities of 468 and 458 mAh $g^{-1}$ after 80 cycles, respectively.[37] Diamondoid-structured Cu-dicarboxylate-based MOF anode for Li-ion storage also was reported, with a reversible capacity being 227 mAh $g^{-1}$ for the first cycle, approximate 95% of the theoretical capacity.[38] A more successful application of formate MOFs for Li storage was reported with a higher capacity (560 mAh $g^{-1}$) that can be retained after 60 cycles.[37] However, the MOF electrodes always decompose during the first electrochemical Li insertion, resulting in a large irreversible loss and poor cycling performance at high current rates.

We hypothesize that it is possible to obtain MOF-type structure which would have good electrochemical performance by incorporating variable-valence metal clusters, such as polyoxometalates instead of molecular species.[40,41] POMs are the building units for designer POM–organic frameworks (POMOFs). They are an interesting subclass of MOFs that exhibit a wide range of magnetic, redox, and catalytic properties.[42–45] However, the use of POMOFs as electrodes in LIBs is still in its infancy.

[a] Chemical Sciences Division, Oak Ridge National Laboratory, Oak Ridge, Tennessee 37831, USA. E-mail: dais@ornl.gov
[b] Department of Biology, Geology, and Physical Science, Sul Ross State University, Alpine, Texas 79832, USA. E-mail: yanfeng.yue@sulross.edu
[c] The Bredesen Center for Interdisciplinary Research and Graduate Education, University of Tennessee, Knoxville, Tennessee 37996, USA.
[d] Materials Science and Technology Division, Oak Ridge National Laboratory, Oak Ridge, Tennessee 37831, USA.
[e] Center for Nanophase Materials Sciences, Oak Ridge National Laboratory, Oak Ridge, Tennessee 37831, USA
[f] Department of Chemistry, University of Tennessee, Knoxville, Tennessee 37996, USA

† Electronic Supplementary Information (ESI) available: [Powder XRD patterns, TGA, and FT-IR curve of as made POMOF-1; cyclic voltammograms of POMOF-1; cycling performance at a current density of 0.25 C; powder XRD patterns of POMOF-1 before and after battery cycling; cycling performance of ligand BDC; cycling performance of $Na_9[A\text{-}\alpha\text{-}PW_9O_{34}]\cdot nH_2O$; $Ni_{3p}$ XPS spectrum.]. See DOI: 10.1039/x0xx00000x

Herein we selectively prepared a POMOF material and for the first time used it as an anode for LIBs. Interestingly, the POMOF anode exhibits an exceptional cycling stability (> 500 times cycling) at a current rate of 1.25C; its stability is possibly due to the flexible POMOF structure. In particular, the flexible framework structure of the POMOF anode material affords an ideal model system for studying the mechanism whereby the variable-valence building units act as active sites of redox reactions.

## 2. Experimental

### 2.1. Synthesis of POMOF-1.

A stoichiometric mixture of $Na_9[A\text{-}\alpha\text{-}PW_9O_{34}]\cdot nH_2O$ (0.30 g)[46] and $NiCl_2\cdot 6H_2O$ (0.80 g, 98%, Aldrich) was stirred in a 0.5M sodium acetate buffer (pH 4.8, 10 mL) for 5 min to form a green colored clear solution. Then 0.30 mL of ethylenediamine was added drop wise with continuous stirring. To this solution $H_2BDC$ (0.20 g) was added and stirred for 120 min. The resulting solution was sealed in a 35 mL stainless steel reactor with a Teflon liner, heated at 170 °C for 5 days, and then cooled to room temperature; after the cooling, green prismatic crystals were obtained. The resulting product was dried under vacuum at 60 °C overnight before further characterizations.

### 2.2. Characterizations.

The FT-IR spectrum of as-made POMOF-1 was recorded by an attenuated total reflection Fourier transform infrared (ATR-FTIR) spectrophotometer (Perkin-Elmer Spectrum One, Perkin-Elmer Co., USA). The spectra were averaged over 16 scans at 4 $cm^{-1}$ resolution obtained in the range of 650–4000 $cm^{-1}$.

Thermogravimetric analysis (TGA) was carried out by using a TA Instrument 2950 from room temperature to 800 °C at a heating rate of 5 °C $min^{-1}$ under air atmosphere.

Powder X-ray diffraction (XRD) analysis was used to confirm the crystallinity as well as the phase purity of the bulk materials. Powder XRD patterns were recorded on a PANalytical Empyrean diffractometer equipped with Cu Kα radiation (λ = 1.5406 Å). Data for the material "as made" were collected in reflection geometry, and typically between 5° to 100° 2θ. Data for the desolvated sample were collected in transmission mode with the sample contained between two mylar sheets to minimize absorption of moisture, typically between the angular range of 3.5° to 85° 2θ. The mylar sheets were sealed with Torr Seal epoxy such that moisture transmission only occurred slowly through the film.

Gas adsorption studies were done to confirm the permanent porosity of the as-synthesized composite sample as well as to determine the surface area. Low pressure gas adsorption experiments were performed on a Micromeritics Tristar 3000 analyzer at 77 K. Around 100 mg as made POMOF-1 was evacuated for 6 hours at 150 °C and subsequently loaded for adsorption analysis.

Electron diffraction and TEM experiments were examined with a Zeiss Libra 120 at 120 kV. An emission current as low as 5μA and minimal exposure times were used to effectively reduce electron-beam-induced sample damage, along with frequent morphology monitoring. Selected area electron diffraction experiments used an aperture size of about 1 micron in diameter and the obtained diffraction patterns were calibrated against a thin film gold standard, assuming the d spacing of Au (111) planes is 0.235 nm.

Surface chemistry was probed using a PHI 3056 XPS spectrometer with Al *K*α radiation (1486.6 eV) at a measurement pressure below $10^{-9}$ Torr. The samples were disassembled in an Ar-filled glovebox and rinsed with anhydrous dimethyl carbonate (Sigma-Aldrich) and transferred under vacuum directly to the XPS sample chamber using an airtight transfer device. High-resolution scans were acquired at 350 W with 23.5 eV pass energy and 0.05 eV energy step. The energy scale of the spectra was calibrated to the C1s peak at 284.8 eV.

The experiments were recorded at the Ni k edge (8333 eV) and the W $L_{III}$ edge (10204 eV) on Beamline X19a at the National Synchrotron Light Source. An Si(111) double crystal monochromator was used and detuned by 30% to reject higher harmonics. The X-ray absorption was measured in transmission. Ion chambers for measuring $I_o$ and $I_t$ were filled with nitrogen and a 50:50 mixture of $N_2$: Ar, respectively. The samples (before/after Li-ion battery cycling) were ground to a fine powder and spread on Kapton tape, which was then folded to produce a uniform thickness and an absorbance, μ(x), of approximately 0.3–0.5. The photon energies were calibrated and aligned by mounting Ni or W foils downstream of the samples. The programs ATHENA and ARTEMIS (available through the DEMETER software package, version 0.9.17) were used to reduce and fit the data, respectively.[47] Data reduction consisted of pre-edge subtraction, background determination, normalization and spectral averaging.

The Raman measurements were carried out using a Renishaw 1000 Raman spectrometer equipped with a 514.5 nm Ar-ion laser, which was focused onto the sample with a 50× objective lens.

### 2.3. Electrochemistry.

Electrochemical experiments were carried out using coin cells. The battery electrode mixtures consisted of 65 wt % active materials, 20 wt % super C45 and 15 wt % polyvinylidene fluoride (PVDF). These materials were ground together by hand and then dispersed in N-methylpyrrolidone to form a slurry. Slurries were deposited onto copper foils and dried at 80 °C for 6 hours, and then further dried under vacuum overnight at 110 °C. The loading of active materials was 1.2 – 1.5 mg $cm^{-2}$. The cells were assembled with 1M $LiPF_6$ in EC/DEC/DMC 1:1:1 vol % electrolyte. The charge discharge experiment was conducted using Land CT2001A with current density of 400 mA $g^{-1}$.

## 3. Results and discussion

The POMOF material, POMOF-1, comprises $\{Ni_6PW_9\}$ structural building units (SBUs) and rigid carboxylate linkers, $\{[Ni_6(OH)_3(H_2O)(en)_3(PW_9O_{34})][Ni_6(OH)_3(H_2O)_4(en)_3(PW_9O_{34})](BDC)_{1.5}\}[Ni(en)(H_2O)_4]\cdot H_3O$ (en = ethylenediamine, $H_2BDC$ = 1,4-benzenedicarboxylic acid); prepared using a hydrothermal method.[48] In the structure, the $\{Ni_6PW_9\}_2$ dimers are interlinked by

linear 1,4-BDC ligands, affording giant parallelogram-shaped rings with dimensions of 2.7 × 3.8 $nm^2$ (Figure 1).[48] Comparison of the powder X-ray diffraction (XRD) patterns for POMOF-1 with those simulated from single-crystal data (Cambridge Crystallographic Data Center, No. CCDC-668400) confirmed that the product was largely phase pure (Figure S1a in supporting information, SI). Rietveld refinement with the program GSAS indicated the presence of a weak impurity with relatively low angle reflections largely overlapped with the main phase (Figure S1b, SI); the impurity peaks could not be assigned using crystallographic databases, suggesting a previous unknown framework material. The as-made material was also characterized by thermal gravimetric analysis (TGA) (Figure S2, SI) and Fourier transform infrared (FT-IR) spectroscopy (Figure S3, SI). The permanent porosity was not detected by the nitrogen adsorption at 77K for the desolvated POMOF-1, indicating the supermolecular framework collapse occurs when the guest molecules between the layers were evacuated (N2 adsorption-desorption isotherms now shown); while the XRD patterns for the desolvated POMOF-1 (Figure S1a, SI) indicate a similar structure for the desolvated form, additional peaks are observed at low angle that cannot be clearly indexed by the solvated cell. Structure solution from powder for the desolvated form of POMOF-1, and identification of the peaks, is ongoing.

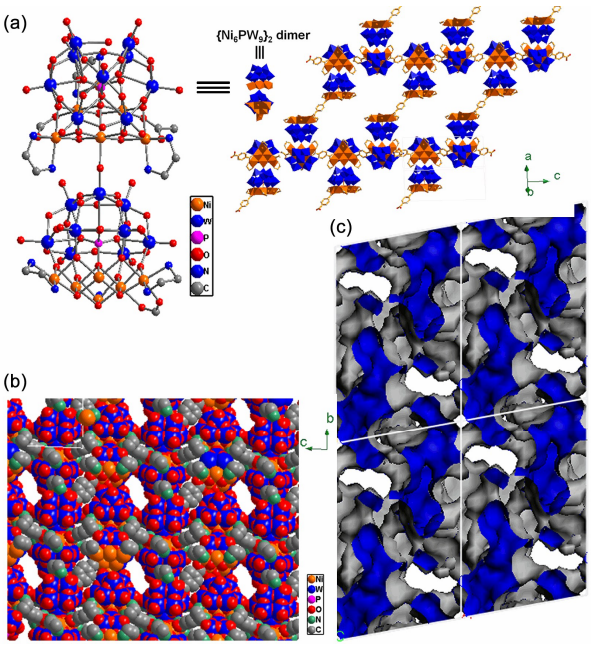


**Figure 1.** Views of $\{(Ni_6PW_9)_2(H_2O)_5\}$ dimer building unit and two-dimensional layer structure in POMOF-1 (a), the space-filling representation of stacking diagram along *a* direction, with the isolated $[Ni(en)(H_2O)_4]^{2+}$ omitted for clarity (b), and Connolly surface representation of the channels, where grey is the outside pores (c).

Cyclic voltammetry (CV) and galvanostatic discharge-charge experiments were conducted to evaluate the Li storage properties of POMOF-1 sample. Figure S4 shows CV curves of POMOF-1 electrode at a scan rate of 0.2 mV/s. There is a small anodic peak at about 1.0 V and a cathodic peak at about 1.2 V in the first cycle. The peak occurring at about 1.0 V might be attributed to the BDC ligands.[38] Figure 2a shows the typical discharge (Li insertion)/charge (Li extraction) profiles for the POMOF-1 anode at a current rate of 1.25C between 5.0 mV to 3.0 V (vs $Li/Li^+$) (the C rate calculation is based on the theoretical capacity of the POMOF-1). The initial discharge and charge capacities were 1421 and 720 mAh $g^{-1}$ (Figure 2a), respectively, giving the first cycle columbic efficiency (CE) of 50.6%, owing to the side-reaction associated with electrolyte decomposition and irreversible reactions of functional groups with Li ions.[49,50] However, after the first few cycles, the CE quickly improved to above 99%, suggesting that a stable SEI could be formed. The POMOF-1 electrode had a reversible capacity of around 350 mAh $g^{-1}$ after 500 cycles (Figure 2b). At a current density of 0.25C, the initial discharge and charge capacities of the POMOF-1 electrode were 1525 and 948 mAh $g^{-1}$, respectively, giving a first cycle CE of 62.2% (Figure S5, SI). After 360 cycles, the reversible capacity was still kept at 540 mAh $g^{-1}$, which is much larger than the commercial anode material graphite. The POMOF-1 anode exhibits a slight capacity fade in the beginning followed by an increase thereafter until becoming stable, which suggests that there is an activation process.[51] It is noticeable the slower rate cycling showed more significant capacity increasing between 25 to 100 cycles, which is possibly attributed to more potential pores activated under lower current rate (Figure S5, SI).

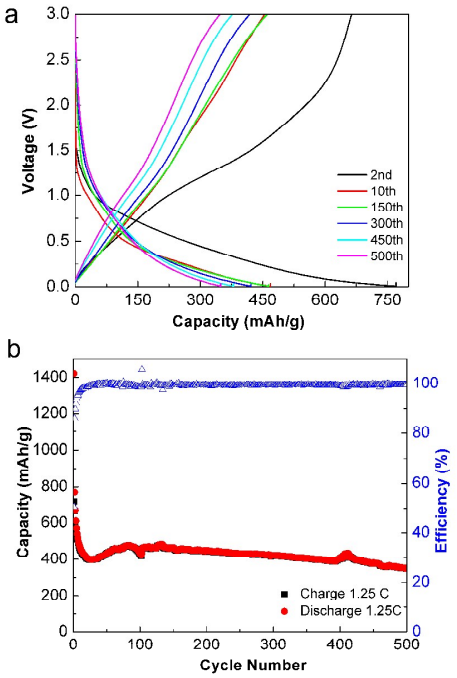


**Figure 2.** Charge–discharge voltage profiles (a) and long cycling performance between 5 mV and 3 V vs $Li^+/Li$ at a current density of 1.25C (b). The C rate calculation is based on the actual experiments in which the cell average capacity can be charged/discharged in 1 hour).

Interestingly, the discharge and charge capacities of the POMOF-1 electrode are much higher than the expected theoretical value (320 mAh $g^{-1}$) based on the following redox reactions which would result in metallic Ni[52] and lithium terephthalate.[36,53] This indicates the probable formation of other species such as $Li_9(PW_{12}O_{34})$ and/or other undetectable materials produced during the cycling.

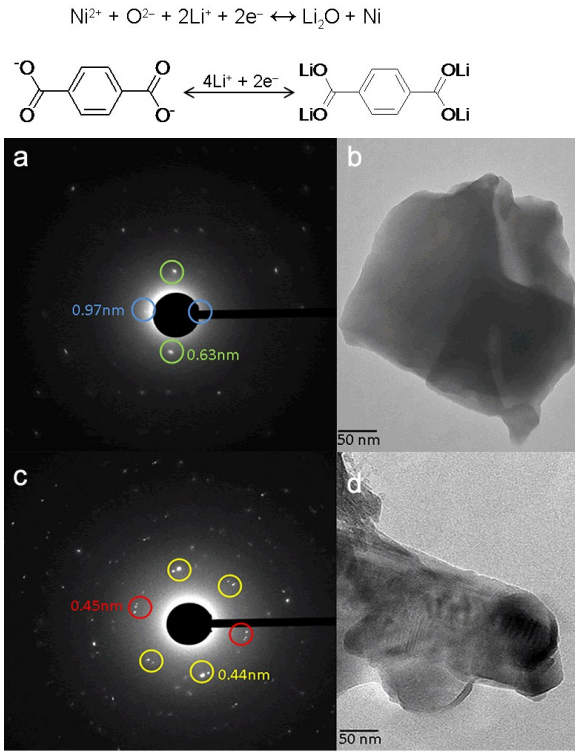


**Figure 3**. Electron diffraction (a) and microstructures (b) of POMOF-1 anode combined with super C45 and polyvinylidene fluoride (PVDF), before Li-ion cycling. Electron diffraction (c) and microstructures (d) of POMOF-1 anode combined with super C45 and polyvinylidene fluoride (PVDF) after Li-ion cycling, with vertical fringes around 2.5 nm.

To explore this reaction further extensive characterization studies were performed. The high-resolution transmission electron microscopy (HRTEM) images show that the blend has a good POMOF-polymer adhesion before charging and discharging cycles. Single crystal diffraction patterns with d spacings of 0.97 nm (020) and 0.63 nm (004) are obtained, which agrees well with the frequent observations of large cube-containing assemblies (**Figure 3**). During charge-discharge cycling, the polymer and POMOF crystals begin to separate; this enables direct lattice imaging of POMOF crystals, and suggests that a possible reason for the capacity decay is loss of electrical contact. The nearly vertical fringes in Figure 4d are measured to be 2.5 nm after cycling the sample, which is attributed to the POMOF-1's (001) spacing. The corresponding selected area diffraction patterns show weaker, overlapping reflections from POMOF crystals with smaller grain dimensions.

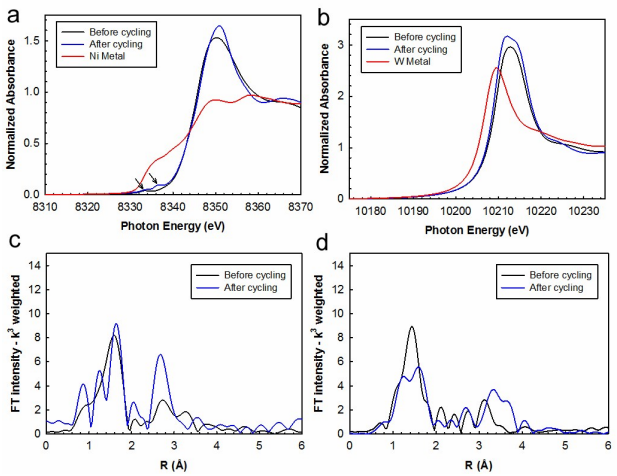


**Figure 4.** Nickel (Ni) (a) and tungsten (W) (b) XANES spectra for POMOF-1 before and after LIB cycling. Ni (c) and W (d) EXAFS spectra of POMOF-1 before and after Li-ion battery cycling.

After the first cycle, the crystalline POMOF-1 anode converted into an amorphous phase (see XRD patterns in Figure S6, SI); however a high capacity was observed, which may be due to the local coordination geometries surrounding the metal ions surviving during the lithiation and delithiation process. This coordination geometry evolution of the local structure after LIB cycling was surveyed with X-ray absorption near edge structure (XANES) and extended X-ray absorption fine structure (EXAFS) studies. The electrode material was extracted from the cell after cycling 10 times, followed by charging to 3 V and holding for 48 hours to ensure maximum delithiation. In the XANES, at both edges, the edge positions were shifted to higher energy than the metal reference. This is an indicative of oxidized nickel (Ni) and tungsten (W). The intensity of the "white line" peak near 8350 eV in the Ni XANES was slightly more intense in the sample after LIB cycling, indicating an increased oxidation. Similar behavior was observed in the W XANES near 10213 eV (Figure S6, SI). Two pre-edge features were evident in the Ni XANES at 8333 eV and 8336.5 eV (see arrows in **Figure 4a**), associated 1s→3d and 1s→4$p_z$ transitions, respectively. The 8333 eV peak is indicative of Ni having six oxygen (O) neighbors in a near octahedral geometry. The 8336.5 eV peak, which emerged after cycling, suggests a lowering of symmetry to form either square planar or tetrahedral geometries.[54,55] In the W XANES the most important feature is the shape of the peak near 10213 eV (Figure 4b). A single peak is indicative of a near octahedral configuration of the O around the W; whereas a doublet, which again emerges after cycling, indicates a distortion of the octahedral geometry.[56] In the EXAFS spectra, the peak(s) between 1–2 Å are from the Ni(W)–O bonds (Figure 4c,d). In the Ni EXAFS spectrum of the sample before cycling, the Ni–O region was fit to six O neighbors at a distance of 2.045 Å. In the W EXAFS spectrum the W–O region was fit to four O neighbors at 1.80 Å and two O neighbors at 2.09 Å. In both the Ni and W EXAFS from the samples after cycling there is still strong O-metal scattering present but the spectra could not be fit to a limited number of O-metal scattering pairs. This suggests that the O geometry around the Ni(W) centers has become much more distorted compared with the samples before cycling. From the combined results of XANES and EXAFS, we conclude that the coordination geometries surrounding the metal ions had a greater distortion after cycling; however the local

structure had largely survived with only a small change in the oxidation state.

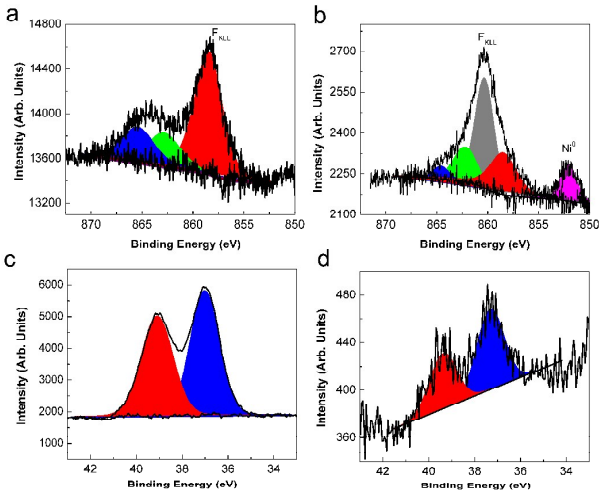


**Figure 5.** Ni2p (top) and W4f (bottom) XPS data collected, along with curve fits, on the as-prepared electrode (left) and lithiated electrode (right). The after cycling material was obtained after the cell cycled for 10 times and discharged to 5 mV and held for 48 hours; the coin cell was opened in a glove box and did not be exposed to air before XPS measurements.

The open framework POMOF anode material differs from traditional electrode materials (e.g., $LiCoO_2$) in that they contain variable-valence metal cluster SBUs; nonetheless, the interconversion of oxidation states of Ni is expected to occur during LIB cycling. If this is the case, some difference in the surface properties of the coatings might be observable. To test this hypothesis, X-ray photoelectron spectroscopy (XPS) studies as well as Raman spectra were carried out to detect the difference in the surface properties of the coated electrode. For the XPS measurements, the electrode material was obtained after the cell was cycled for 10 times, followed by discharging to 5 mV (lithiation) and holding for 48 hours. Figure 5 shows the Ni 2p and W4f XPS data collected for the as-prepared and lithiated electrodes. For both samples, the W4f XPS data showed a W4f7/2 binding energy around 37 eV, which was consistent with the presence of $W^{6+}$ on the surface of the electrode material. Furthermore, since there was no change in the W4f binding energy with lithiation, it would indicate that the W is electrochemically inactive. The Ni 2p XPS data collected for the uncycled electrode showed the presence of a large signal centered around 858.5 eV. This large feature was due to the $F_{KLL}$ Auger line originating from the F in the PVDF binder. The Ni 2p spectra coincides with this F Auger line, indicating the Ni has an oxidation state greater than or equal to 2+. To confirm this result, the Ni 3p spectra were analyzed (Figure S6, SI). This species shows two peaks due to $Ni3p_{3/2}$ and $Ni3p_{1/2}$ with the $Ni3p_{3/2}$ binding energy around 69.5 eV, which is consistent with a $Ni^{2+}$ type species.[57] After lithiation, there were several pronounced changes in the Ni 2p XPS spectra. First there was the addition of a new species with a binding energy of 852 eV due to the formation of $Ni^0$.[58] This result indicates that the $Ni^{2+}$ is reduced during lithation. There were also clear changes in the $F_{KLL}$ Auger region that originated from additional F species which are trapped in the SEI layer from the decomposition of $LiPF_6$ in addition to the PVDF binder. Indeed, the surface chemistry is dominated by additional F, C, and O species from the SEI layer, which significantly reduces the photoelectrons from Ni and W. Attempts to confirm the Ni oxidation state by investigating the Ni 3p spectra were unsuccessful because of this SEI layer, which effectively attenuated the Ni 3p signal (Figure S7).

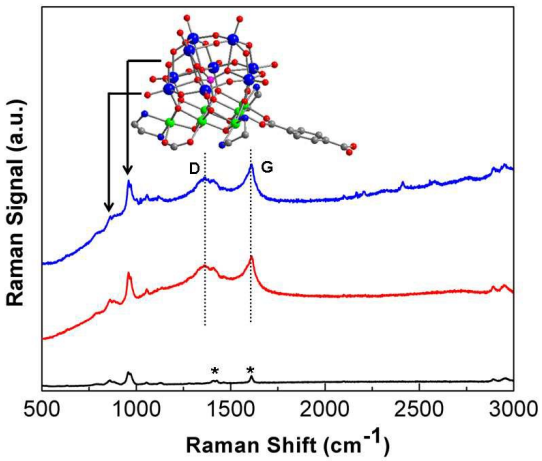


**Figure 6.** Raman spectra of as-made POMOF-1, before and after Li-ion battery cycling. The Raman spectrum (black line) of the as-made POMOF-1 material exhibits the characteristic peaks of aromatic carbon (star denoted); and the Raman spectra of POMOF-1 before (red line) and after (blue) exhibit G and D peaks of C45. The lithiated material was obtained from the cell after cycling 10 times and then discharged to 5m V and held for 48 hours; the cell was opened in glove box and covered with Teflon film. The sample was then transferred to the Raman for examination without any exposure to air.

The $[Ni_6(PW_9O_{34})]$ building units compose significantly distorted edging sharing $WO_6$ fragments and exhibit Raman features at 971 ($\nu_s$(W=O)), 958 ($\nu_{as}$(W=O)) $cm^{-1}$,[59,60] with the characteristic peaks at 1418 and 1600 $cm^{-1}$ for aromatic carbon (Figure 6).[61] The weaker peak at 860 $cm^{-1}$ attributes to the vibrations of the W=O bonds with the O atoms related to the terminal coordinated water molecules. The before- and after-cycling anode materials show two additional Raman features at 1366 and 1609 $cm^{-1}$ related to the *G* and *D* peaks due to the incorporation of C45.[62] Compared with the before-cycling sample, several small peaks appeared in the range of 2200–2700 $cm^{-1}$, perhaps because of the electrolyte complexes obtained after the cycling. No Raman shifts were detected for the before- and after-cycling samples; combined with the incidences in the XANES, EXAFS, and XPS, this provided unambiguous evidence that the local SBU structural motif was retained as the valence of Ni changed during the lithation and delithiation cycling.

## 4. Conclusions

In summary, a crystalline POMOF electrode material—formed with polyoxometalate clusters as SBUs and rigid carboxylate as organic linkers, with a larger interstitial space than the Li ions—was studied as an anode material for LIB, exhibiting a high storage capacity at a high current rate of 1.25C. The studies of X-ray absorption near edge structure, electron

diffraction, and Raman spectra clearly demonstrated that the building units and local structure of this anode material are maintained during lithiation and delithiation processing. This suggests a new route for pursuing LIB electrode materials made from metal coordination polymers by introducing variable-valence POM as a secondary building unit. The present work provides an important framework for expanding the studies of MOFs in the area of electrochemically active materials.

## Acknowledgements

The research was sponsored by the by the U.S. Department of Energy, Office of Science, Basic Energy Sciences, Division of Materials Science and Engineering. Electron diffraction and HRTEM were conducted at the Center for Nanophase Materials Sciences, which is sponsored at Oak Ridge National Laboratory by the Division of Scientific User Facilities, Office of Basic Energy Sciences, U.S. Department of Energy. Battery testing (YL, MPP), XPS work (GMV), and powder diffraction (CB) was supported by the U.S. Department of Energy, Office of Science, Basic Energy Sciences, Division of Materials Science and Engineering.

## References

1 C. Yuan, H. B. Wu, Y. Xie and X. W. Lou,*Angew. Chem. Int. Ed*., 2014, **53**, 1488–1504.
2 S. Yang, X. Feng, S. Ivanovici and K. Müllen, *Angew. Chem. Int. Ed*., 2010, **49**, 8408–8411.
3 N.-S. Choi, Z. Chen, S. A. Freunberger, X. Ji, Y.-K. Sun, K. Amine, G. Yushin, L. F. Nazar, J.; Cho and P. G. Bruce, *Angew. Chem. Int. Ed*., 2012, **51**, 9994–10024.
4 X. Li, M. Gu, S. Hu, R. Kennard, P. Yan, X. Chen, C. Wang, M. J. Sailor, J.-G. Zhang and J. Liu, *Nat. Commun*., 2014, **5**, 4105.
5 J. Li, A. K. Dozier, Y. Li, F. Yang and Y.-T. Cheng, *J. Electrochem. Soc*., 2011, **158**, A689–A694.
6 X. Sun, C. Yan, Y. Chen, W. Si, J. Deng, S. Oswald, L. Liu and O. G. Schmidt, *Adv. Energy Mater*., 2014, **4**, 1300912.
7 X. Huang, H. Yu, J. Chen, Z. Lu, R. Yazami and H. H. Hng, *Adv. Mater*., 2014, **26**, 1296–1303.
8 X.-L. Wang, W.-Q. Han, H. Chen, J. Bai, T. A. Tyson, X.-Q. Yu, X.-J. Wang and X.-Q. Yang, *J. Am. Chem. Soc*., 2011, **133**, 20692–20695.
9 H. Wu, G. Chan, J. W. Choi, I. Ryu, Y. Yao, M. T. McDowell, S. W. Lee, A. Jackson, Y. Yang, L. Hu and Y. Cui, *Nat. Nanotechnol*., 2012, **7**, 311–315.
10 J.-H. Cho and S. T. Picraux, *Nano Lett*., 2013, **13**, 5740–5747.
11 Y.-S. Hu, X. Liu, J.-O. Müller, R. Schlögl, J. Maier and D. S. Su, *Angew. Chem. Int. Ed*., 2009, **48**, 210–214.
12 S.-H. Ng, J. Wang, D. Wexler, K. Konstantinov, Z.-P. Guo and H.-K. Liu, *Angew. Chem. Int. Ed*., 2006, **45**, 6896–6899.
13 Y. Chen, X. Li, K. Park, J. Song, J. Hong, L. Zhou, Y.-W. Mai, H. Huang and J. B. Goodenough, *J. Am. Chem. Soc*., 2013, **135**, 16280–16283.
14 E. Kang, Y. S. Jung, A. S. Cavanagh, G.-H. Kim, S. M. George, A. C. Dillon, J. K. Kim and J. Lee, *Adv. Funct. Mater*., 2011, **21**, 2430–2438.
15 D. R. MacFarlane and M. Forsyth *Adv. Mater*., 2001, **13**, 957–966.
16 J. Luo, A. H. Jensen, N. R. Brooks, J. Sniekers, M. Knipper, D. Aili, Q. Li, B. Vanroy, M. Wübbenhorst, F. Yan, L. Van Meervelt, Z. Shao, J. Fang, Z.-H. Luo, D. E. De Vos, K. Binnemans and J. Fransaer, *Energy Environ. Sci*., 2015, **8**, 1276–1291
17 E. Coronado and C. J. Gómez-García, *Chem. Rev*., 1998, **98**, 273–296.
18 L.-W. Han, J.-X. Lin, J. Lü and R. Cao, *Dalton Trans*., 2012, **41**, 10080–10084.
19 X. Qian, X. Tong, Q. Wu, Z. He, F. Cao and W. Yan, *Dalton Trans*., 2012, **41**, 9897–9900.
20 A. Morozan and F. Jaouen, *Energy Environ. Sci*., 2012, **5**, 9269–9290.
21 G. de Combarieu, M. Morcrette, F. Millange, N. Guillou, J. Cabana, C. P. Grey, I. Margiolaki, G. Férey and J.-M. Tarascon, *Chem. Mater*., 2009, **21**, 1602–1611.
22 S.-L. Li and Q. Xu, *Energy Environ. Sci*., 2013, **6**, 1656–1683.
23 N. T. T. Nguyen, H. Furukawa, F. Gándara, H. T. Nguyen, K. E. Cordova and O. M. Yaghi, *Angew. Chem. Int. Ed*., 2014, **53**, 10645–10648.
24 Y. Cui, Y. Yue, G. Qian and B. Chen, *Chem. Rev*., 2012, **112**, 1126–1162.
25 S. Furukawa, K. Hirai, Y. Takashima, K. Nakagawa, M. Kondo, T. Tsuruoka, O. Sakata and S. Kitagawa, *Chem. Commun*., 2009, 5097–5099.
26 O. K. Farha, C. E. Wilmer, I. Eryazici, B. G. Hauser, P. A. Parilla, K. O'Neill, A. A. Sarjeant, S. T. Nguyen, R. Q. Snurr and J. T. Hupp, *J. Am. Chem. Soc*., 2012, **134**, 9860–9863.
27 B. Moulton and M. J. Zaworotko, *Chem. Rev*., 2001, **101**, 1629–1658.
28 J. R. Li, R.-J. Kuppler and H.-C. Zhou, *Chem. Soc. Rev*., 2009, **38**, 1477–1504.
29 Z. Xin, J. Bai, Y. Pan and M. J. Zaworotko, *Chem. Eur. J*., 2010, **16**, 13049–13052.
30 T. Ben, C. J. Lu, C. Y. Pei, S. X. Xu and S. L. Qiu, *Chem. Eur. J*., 2012, **18**, 10250–10253.
31 S. T. Zheng, T. Wu, C. T. Chou, A. Fuhr, P. Y. Feng and X. H. Bu, *J. Am. Chem. Soc*., 2012, **134**, 1934–1937.
32 Y. Yue, Z.-A. Qiao, P. F. Fulvio, A. J. Binder, C. Tian, J. Chen, K. M. Nelson, X. Zhu and S. Dai, *J. Am. Chem. Soc*., 2013, **135**, 9572–9575.
33 V. Lykourinou, Y. Chen, X.-S. Wang, L. Meng, T. Hoang, L.-J. Ming, R. L. Musselman and S. Ma, *J. Am. Chem. Soc*., 2011, **133**, 10382–10385.
34 C. Liu, T. Li and N. L. Rosi, *J. Am. Chem. Soc*., 2012, **134**, 18886–18888.
35 P. K. Thallapally, J. Tian, M. R. Kishan, C. A. Fernandez, S. J. Dalgarno, P. B. McGrail, J. E. Warren and J. L. Atwood, *J. Am. Chem. Soc*., 2008, **130**, 16842–16843.
36 M. Armand, S. Grugeon, H. Vezin, S. Laruelle, P. Ribière, P. Poizot and J.-M. Tarascon, *Nat. Mater*., 2009, **8**, 120–125.
37 X. Han, F. Yi, T. Sun and J. Sun, *Electrochem. Commun*., 2012, **25**, 136–139.
38 R. S. Kumar, C. Nithya, S. Gopukumar and M. A. Kulandainathan, *Energy Technol*., 2014, **2**, 921– 927.
39 K. Saravanan, M. Nagarathinam, P. Balaya and J. J. Vittal, *J. Mater. Chem*., 2010, **20**, 8329–8335.
40 Nyman, M. *Dalton Trans*., 2011, **40**, 8049–8058.
41 N. Sun, X. Jiang, M. L. Maxim, A. Metlen and R. D. Rogers, *ChemSusChem,* 2011, **4**, 65–73.
42 C.-Y. Sun, S.-X. Liu, D.-D. Liang, K.-Z. Shao, Y.-H. Ren and Z.-M. Su, *J. Am. Chem. Soc*., 2009, **131**, 1883–1888.
43 L. M. Rodriguez-Albelo, A. R. Ruiz-Salvador, A. Sampieri, D. W. Lewis, A. Gómez, B. Nohra, P. Mialane, J. Marrot, F. Sécheresse, C. Mellot-Draznieks, R. N. Biboum, B. Keita, L. Nadjo and A. Dolbecq, *J. Am. Chem. Soc*., 2009, **131**, 16078–16087.
44 T. Yu, H. Ma, C. Zhang, H. Pang, S. Li and H. Liu, *Dalton Trans*., 2013, **42**, 16328–16333.
45 L. M. Rodriguez Albelo, A. R. Ruiz-Salvador, D. W. Lewis, A. Gómez, P. Mialane, J. Marrot, A. Dolbecq, A. Sampierie and

C. Mellot-Draznieks, *Phys Chem Chem Phys*., 2010, **12**, 8632–8639.
46 A. P. Ginsberg, *Inorganic Syntheses*, Wiley, New York, 1990, **27**, 85.
47 B. Ravel and M. Newville, *J. Synchrotron Radiat*., 2005, **12**, 537–541.
48 S.-T. Zheng and J. Zhang, G.-Y. Yang, *Angew. Chem. Int. Ed*., 2008, **47**, 3909–3913.
49 E. Buiel, J. R. Dahnt, *J. Electrochem. Soc*., 1998, **145**, 1977–1981.
50 J. B. Goodenough and Y. Kim, *Chem. Mater*., 2010, **22**, 587–603.
51 J. Zheng, J. Tian, D. Wu, M. Gu, W. Xu, C. Wang, F. Gao, M. H. Engelhard, J.-G. Zhang, J. Liu and J. Xiao, *Nano Lett*., 2014, **14**, 2345–2352.
52 P. Poizot, S. Laruelle, S. Grugeon, L. Dupont and J.-M. Tarascon, *Nature*, 2000, **407**, 496–499.
53 X. Wu, S. Jin, Z. Zhang, L. Jiang, L. Mu, Y.-S. Hu, H. Li, X. Chen, M. Armand, L. Chen and X. Huang, *Sci. Adv*., 2015, **1**, e1500330.
54 G. J. Colpas, M. J. Maroney, C. Bagyinka, M. Kumar, W. S. Willis, S. L. Suib, N. Baidya, P. K. Mascharak and N. Baidya, *Inorg. Chem*., 1991, **30**, 920–928.
55 S. B. Choudhury, J.-W. Lee, G. Davidson, Y.-I. Yim, K. Bose, M. L. Sharma, S.-O. Kang, D. E. Cabelli and M. J. Maroney, *Biochem*., 1999, **38**, 3744–3752.
56 S. Yamazoe, Y. Hitomi, T. Shishido and T. Tanaka, *J. Phys. Chem. C,* 2008, **112**, 6869–6879.
57 G. Ertl, R. Hierl, H. Knozinger, N. Thiele and H. P. Urbach, *Appl. Surf. Sci*., 1980, **5**, 49–64.
58 N. W. Cheung, P. J. Grunthaner, F. J. Grunthaner, J. W. Mayer and B. M. Ullrich, *J. Vac. Sci. Technol*., 1981, **18**, 917–923.
59 S.-H. Lee, H. M. Cheong, N.-G. Park, C. E. Tracy, A. Mascarenhas, D. K. Benson and S. K. Deb, *Solid State Ionics*, 2001, **140**, 135–139.
60 E. Cazzanelli, C. Vinegoni, G. Mariotto, A. Kuzmin and J. Purans, *Solid State Ionics*, 1999, **123**, 67–74.
61 R. Rumelfanger, S. A. Asher and M. B. Perry, *Appl. Spectrosc.,* 1988, **42**, 267–272.
62 Y. Wang, D. C. Alsmeyer and R. L. McCreery, *Chem. Mater*., 1990, **2**, 557–563.

**TOC**

A polyoxometalate-organic framework with multiple valence polyoxometalate clusters as redox active building units demonstrated as anode material for Li-ion batteries.